Microporosity of heat-treated manganese dioxide

J.B. Arnott [a], R.P. Williams [b], A.G. Pandolfo [c], S.W. Donne [a,*]

[a] *Discipline of Chemistry, University of Newcastle, Callaghan, NSW 2308, Australia*
[b] *Delta EMD Australia Pty Limited, McIntosh Drive, Mayfield West, NSW 2304, Australia*
[c] *CSIRO Division of Energy Technology, Bayview Avenue, Clayton, Victoria 3169, Australia*

Available online 20 November 2006

Abstract

A structural and micro-pore analysis of a series of heat treated electrolytic manganese dioxide (EMD) samples has been conducted. In terms of crystal structure, the original EMD with γ-MnO$_2$ structure (orthorhombic unit cell) was found to progressively convert to β-MnO$_2$ (tetragonal unit cell) at elevated temperatures. The structural transition was kinetically limited, with the higher temperatures leading to a greater degree of transformation. The orthorhombic γ-MnO$_2$ unit cell was found to contract along the *a* and *b* axes, while along the *c* axis an expansion was observed only at the highest heat treatment temperatures. These changes occur as a result of manganese ion diffusion leading to the formation of a denser, more defect free material. The porosity of these heat treated EMD samples was also examined by N$_2$ gas adsorption combined with various interpretive techniques such as the Kelvin equation, MP method, Dubinin–Radushkevich method, Dubinin–Astakhov method and a more modern density functional theory based approach. Despite shortcomings associated with certain techniques, all clearly indicated that the EMD micro-pore volume decreased and the meso- and macro-pore volume increased as the heat treatment temperature was increased. This was justified as a result of manganese ion movement during the structural rearrangement causing the small pores to be progressively sintered shut, while the larger pores were formed as a result of stress-induced cracking in the denser final product.
© 2006 Elsevier B.V. All rights reserved.

Keywords: Electrolytic manganese dioxide; EMD; Porosity

1. Introduction

1.1. Background

Manganese dioxide has for over 50 years been used as the cathode active material in primary batteries. This widespread popularity is due to a unique combination of its physicochemical and electrochemical properties, including its relatively high density and purity, its ability to adequately maintain up to and including intermediate discharge rates for prolonged periods of time (particularly when used in concentrated alkaline electrolytes), as well as the fact that it is environmentally benign when disposed. Add to that the inexpensive nature of the raw materials necessary to prepare manganese dioxide, leads to it being a very difficult material to supercede. Despite many years

of usage and research into its behaviour there are still many properties of manganese dioxide that are unclear and need clarification. One of these is the role of manganese dioxide porosity, which is the subject of this work.

1.2. Manganese dioxide structures and morphology

As a compound, manganese dioxide has a wide array of different crystal structures, so much so that over 30 different species have been classified [1]. The importance of structure is that it influences dramatically the electrochemical behaviour of the material. It is therefore essential that we describe in some detail the structures we will encounter in this work.

Manganese in oxidation states II, III and IV prefers almost exclusively an octahedral coordination, albeit somewhat distorted. This is particularly true for Mn(III) containing species, since it is a Jahn–Teller distorted ion. Therefore, the basic building block for the majority of manganese oxides and hydroxides is the [Mn(O^{2-},OH$^-$,OH$_2$)$_6$]$^{z+}$ octahedral unit. Various corner and/or edge sharing assemblages of these octahedral units give rise to different structures [2]. An alternative approach to interpreting manganese oxide structures is to visualize a

* Corresponding author.
E-mail addresses: jeremy.arnott@studentmail.newcastle.edu.au
(J.B. Arnott), williams.rodney.rp@deltaemd.com.au (R.P. Williams),
tony.pandolfo@csiro.au (A.G. Pandolfo), scott.donne@newcastle.edu.au
(S.W. Donne).

hexagonal close-packed array of oxide anions, into which manganese cations are placed selectively into the octahedral sites.

The simplest manganese dioxide structure is that of β-MnO$_2$ (pyrolusite) which consists of corner sharing octahedra in the *a–b* plane, and edge sharing octahedra in the *c* direction. The result is a [1 × 1] tunnel structure progressing in the *c* direction, as shown in Fig. 1(a). For this tetragonal structure the unit cell parameters are $a_0 = 0.439$ nm and $c_0 = 0.287$ nm [1]. In a similar way, the structure of ramsdellite can be visualized, this time though with both edge and corner sharing in the *a–b* plane to form a [2 × 1] tunnel headed into the *c* direction. Ramsdellite has an orthorhombic unit cell with $a_0 = 0.446$ nm, $b_0 = 0.932$ nm and $c_0 = 0.285$ nm [1]. A schematic of its structure is shown in Fig. 1(b).

The preferred phase for use in the alkaline manganese dioxide cathode is γ-MnO$_2$. The basis for describing the γ-structure is as a random microscopic intergrowth between both the pyrolusite and ramsdellite structures of manganese dioxide [3], as shown in Fig. 1(c). Other features associated with the γ-MnO$_2$ structure include cation vacancies, lower valent manganese cations (Mn(III)), and structural water present as protons associated with oxide anions so as to compensate for the charge deficiency

incurred by cation vacancies and Mn(III) ions [4]. As a result, the chemical composition of γ-MnO$_2$ has been described as

$$(Mn^{4+})_{1-x-y} \cdot ([])_x \cdot (Mn^{3+})_y \cdot (O^{2-})_{2-4x-y} \cdot (OH^-)_{4x+y} \qquad (1)$$
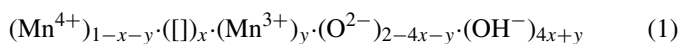
where x and y represent the mole fraction of cation vacancies ([]) and Mn(III) ions, respectively. Typical ranges for x and y in an unreduced γ-MnO$_2$ sample are 0.06–0.08 and 0.04–0.12, respectively. Another structural component of γ-MnO$_2$ that has been proposed is microtwinning in the (0 2 1) and (0 6 1) growth planes. Structural modeling including microtwinning has been used to explain the appearance of certain features in the X-ray diffraction pattern of γ-MnO$_2$; however, there is conflicting physical evidence as to its actual existence [5,6].

Clearly, based on the currently accepted structural and chemical (Eq. (1)) definition, there can be a multitude of materials loosely classified as γ-MnO$_2$, even though their structural, and to some extent chemical, composition can vary considerably. There are many synthetic routes leading to γ-MnO$_2$, each with their own list of experimental variables that can alter its structural and chemical composition as defined above. However, the γ-MnO$_2$ used as the cathode-active material in alkaline cells is most often prepared using electrolytic means (electrolytic manganese dioxide, EMD) [7], which in itself imparts a unique morphology to the material. The original high resolution TEM work on EMD was conducted by Turner and Buseck [8], and it showed definitive evidence in support of De Wolff's microscopic intergrowth model for γ-MnO$_2$ [3]. More recent TEM work on EMD by Heuer et al. [9] has shown the material to consist of needle-like crystallites ∼10 nm × 10 nm × 100 nm in size. These needles were then found to be assembled in a somewhat ordered fashion into grains ∼200 nm in diameter. These grains were then found to be arranged randomly to form the bulk structure. Also apparent between the crystallites and grains were pores, into which electrolyte is expected to permeate during electrochemical discharge. It is these pores, their size and distribution, that we intend to characterize in this work.

1.3. The importance of porosity

Before discussing manganese dioxide porosity it is important to emphasize why it is so important. As mentioned above, the structural variety of manganese dioxide preferred for use in alkaline Zn/MnO$_2$ cells is γ-MnO$_2$. As a cathode active material, γ-MnO$_2$ undergoes electrochemical reduction according to

$$MnOOH_r + \Delta H_2O + \Delta e^- \rightarrow MnOOH_{r+\Delta} + OH^- \qquad (2)$$
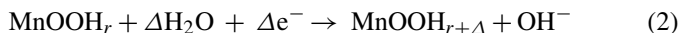
where r is the mole fraction of hydrogen (H$^+$/e$^-$ pairs) present in the starting material ($r \approx 0.1$ in an unreduced sample), and Δ indicates the mole fraction of hydrogen inserted during reduction [10]. This is a homogeneous reduction process for the majority of the discharge in concentrated alkaline electrolytes; i.e., down to $r + \Delta \approx 0.8$ [11]. The reduction itself involves electron injection from the external circuit (via the conductive graphite chain) into the manganese dioxide structure to reduce Mn(IV) to Mn(III), together with proton insertion at the manganese dioxide-electrolyte interface as a result of water decomposition.
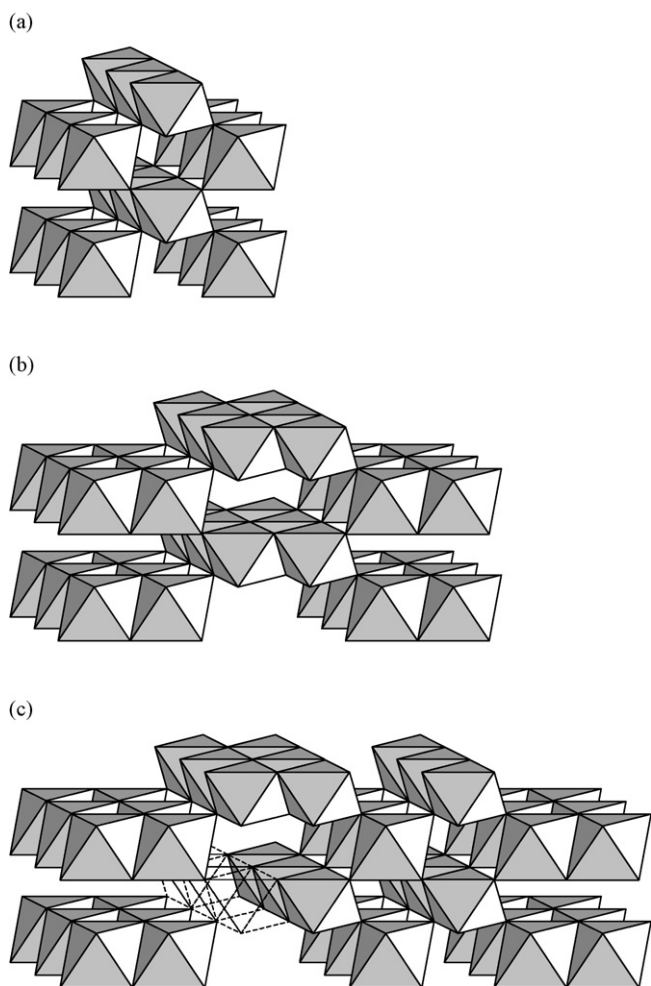

Fig. 1. Schematic representations of: (a) the pyrolusite (β-MnO$_2$), (b) the ramsdellite, and (c) the γ-MnO$_2$ structures.
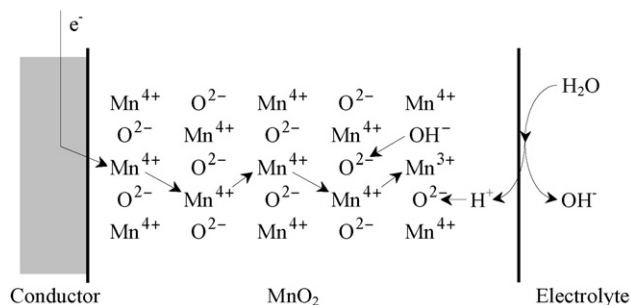
Fig. 2. Schematic of the γ-MnO₂ reduction mechanism.

Once inserted, the H⁺/e⁻ pairs diffuse under an activity gradient to achieve a uniform distribution throughout the structure (Fig. 2). Given that proton transport is widely believed to be the rate limiting property in the discharge of manganese dioxide [12], the facility with which protons are inserted into the structure is a key electrochemical property. Inherent with this is of course the size of the manganese dioxide–electrolyte interface, which is for the most part associated with pores.

1.4. This work

Our approach in this study has been to examine the changes in porosity that occur when a sample of electrolytic manganese dioxide (EMD) is subjected to a variety of heat treatment temperatures. Our intention is to begin to understand how physical changes in the structure of the material influence its morphology.

2. Experimental

2.1. Material synthesis and characterization

The starting material used in this work was a standard commercial EMD provided by Delta EMD Australia Pty Limited. It was prepared by anodic electrolysis of a hot (~98 °C), acidic (H_2SO_4) solution of $MnSO_4$ onto a titanium substrate. After deposition the EMD was mechanically removed from the anode substrate, milled into a −105 μm powder, washed, neutralized and then dried before being ready for use.

Sub-samples of this starting material were then taken and subjected to heat treatment in air at temperatures from 100 up to 400 °C (in 100 °C increments). The duration of the heat treatment was 24 h.

Structural information was obtained on the materials using X-ray diffraction (XRD). A Philips PW1710 diffractometer equipped with a Cu Kα source was used. Patterns were recorded over the 2θ range 10–80° with a step size of 0.05° and a count time of 2.5 s.

Morphological information on each sample was obtained through the use of a Philips XL30 scanning electron microscope (SEM).

2.2. Porosity determination

Sample porosity was determined from gas adsorption/desorption isotherms collected using a Micromeritics ASAP 2010 Surface Area and Porosity system, adapted with a turbo-molecular pump to examine low pressure adsorption. Prior to analysis, samples were out-gassed under vacuum at 110 °C for 2 h to remove surface water which would otherwise interfere with the measurement. N_2 adsorption and desorption isotherms were then collected at 77 K.

3. Results and discussion

3.1. Crystal structure and morphology

X-ray diffraction is the most common tool used to characterize the crystal structure of manganese dioxide. However, despite its widespread use, various forms of manganese dioxide tend to be finely divided and disordered meaning that their XRD patterns often contain broad peaks which overall makes the technique of powder XRD less useful. Nevertheless, the structural modeling work conducted by Chabre and Pannetier [5] does allow us to shed some light on the structure of EMD from its XRD pattern.

XRD patterns of the samples prepared in this work are shown in Fig. 3, with the pattern for EMD labeled with the corresponding Miller indices assuming an orthorhombic unit cell [5]. The most obvious changes occurring as a result of heat treatment are (i) merging of the (1 1 0) (~22°2θ) and the (1 3 0) (~36°2θ) lines in the EMD (γ-MnO₂) starting material to form a single peak at ~29°2θ for the 400 °C heat treated sample; (ii) clearer separation of the (2 2 1) and (2 4 0) lines at ~56°2θ by 400 °C;
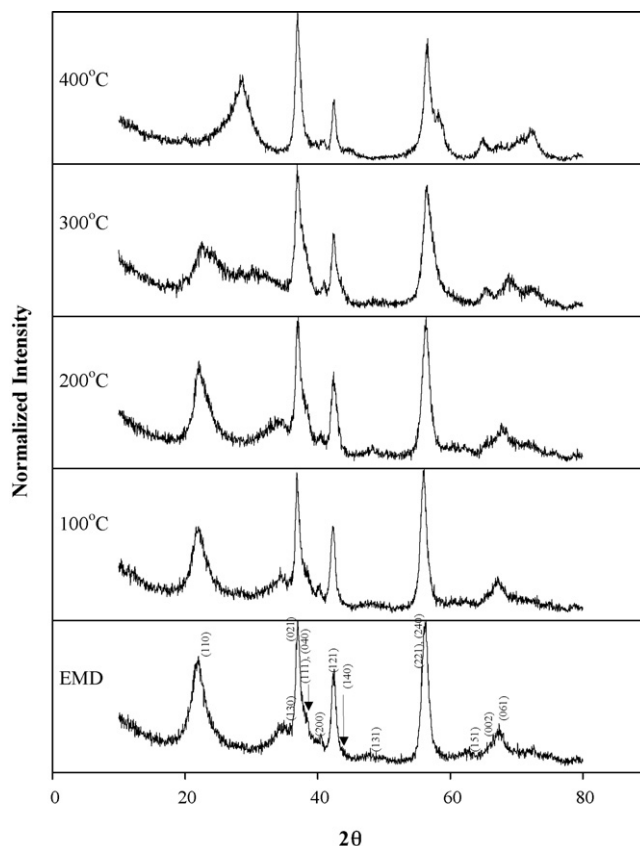

Fig. 3. XRD patterns of heat-treated EMD.

and (iii) disappearance of the line at ∼68°2θ, with the corresponding emergence of two lines at ∼65°2θ and ∼73°2θ. These observations concerning the XRD pattern are consistent with previous works [13] in the sense that they indicate the progressive conversion of γ-MnO$_2$, with a predominantly ramsdellite structural composition, into pyrolusite or β-MnO$_2$. To quantify this change, the approach developed by Chabre and Pannetier [5] for XRD pattern analysis has been adopted to determine the fraction of pyrolusite in the γ-MnO$_2$ structure (P_r), as shown in Fig. 4. What is most significant is that even at relatively low temperatures, and after only 24 h at temperature, the γ-MnO$_2$ structure has already begun to convert to pyrolusite.

This can be reinforced further by considering the changes in unit cell parameters (extracted from the XRD patterns) as a function of temperature. For the EMD sample used in this work its unit cell parameters were determined to be $a_0 = 0.4475$ nm, $b_0 = 0.9676$ nm and $c_0 = 0.2825$ nm, which is slightly expanded in the a–b plane, but contracted along the c axis compared to ramsdellite. The most convenient way to demonstrate how the structure changes with heat treatment was to determine the difference between the unit cell parameters of the heat treated samples and the starting EMD, as shown in Fig. 5. As shown, both the a_0 and b_0 parameters decrease progressively, essentially from the outset of heat treatment. However, c_0 remains relatively constant throughout most of the temperature range studied, increasing substantially only at 400 °C. If we consider the respective γ- and β-MnO$_2$ structures, as shown in Fig. 1, the main differences are apparent in the a–b crystallographic plane. The fact that the unit cell contracts along the a and b axes suggests that ion (Mn^{4+}) movement in these directions predominates during heat treatment, so as to ultimately form a denser, more defect free structure. Along the c axis, the structural expansion at 400 °C may be due to an excess of edge sharing octahedra in
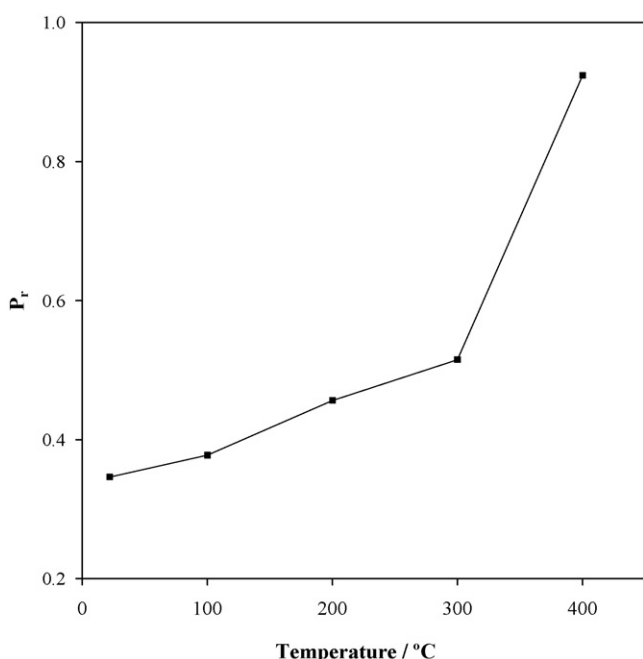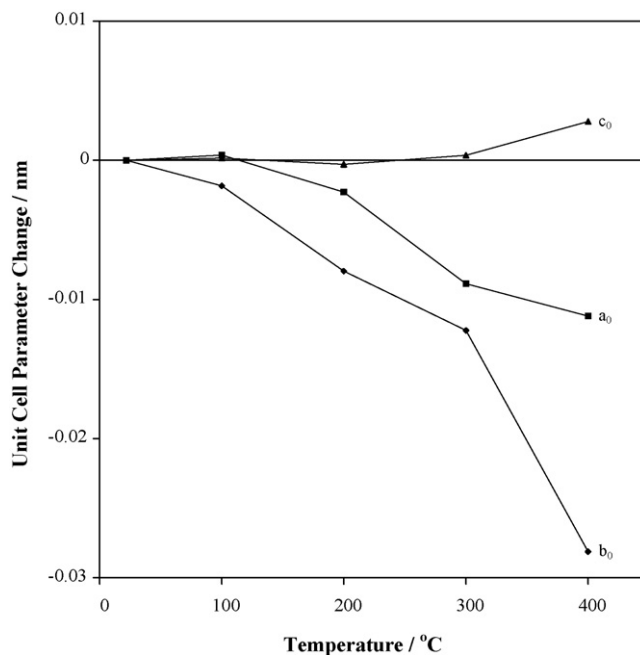

Fig. 5. Changes in unit cell parameters as a function of heat treatment temperature.

a uniform array, without the presence of defects such as cation vacancies to compensate or provide a buffer for the close proximity of the Mn^{4+} ions.

SEM images of the 100 and 400 °C heat treated EMD samples are shown in Fig. 6. These images are of the surface of a much larger particle, and demonstrate that both samples are composed of agglomerates of small grains less than ∼100 nm in size, which is still much larger than the average crystallite (primary particle) size calculated from the Scherrer equation [14] using the XRD data in Fig. 3; i.e., ∼14 nm, suggesting that these grains are also agglomerates. It is also apparent that there is very little difference in morphology between these two samples, indicating that heat treatment has little effect on morphology in this size range.

3.2. Gas adsorption/desorption isotherms

An example of a typical gas adsorption and desorption isotherm collected in this work is shown in Fig. 7. Both the adsorption and desorption isotherms were as expected, particularly the desorption isotherm which demonstrated a substantial hysteresis loop in the P/P_0 range above 0.4. This is believed due to the slower than expected evaporation from the surface as a result of surface tension phenomena associated with the liquefied adsorbate [15]. Furthermore, at relative pressures greater than 0.9, the rapid increase in the volume of adsorbed gas is due to condensation of the adsorbate in the larger "pores" formed between particles. This has been shown to be the case as a result of studies on different particle size distributions of the same material [15]. At very low relative pressures below $P/P_0 = 0.1$, the adsorbate shows a high affinity for the solid surface, approaching zero only at relative pressures of ∼10^{-6}. Needless to say, gas adsorption in pores contributes substantially to the adsorption behaviour at these relative pressures.

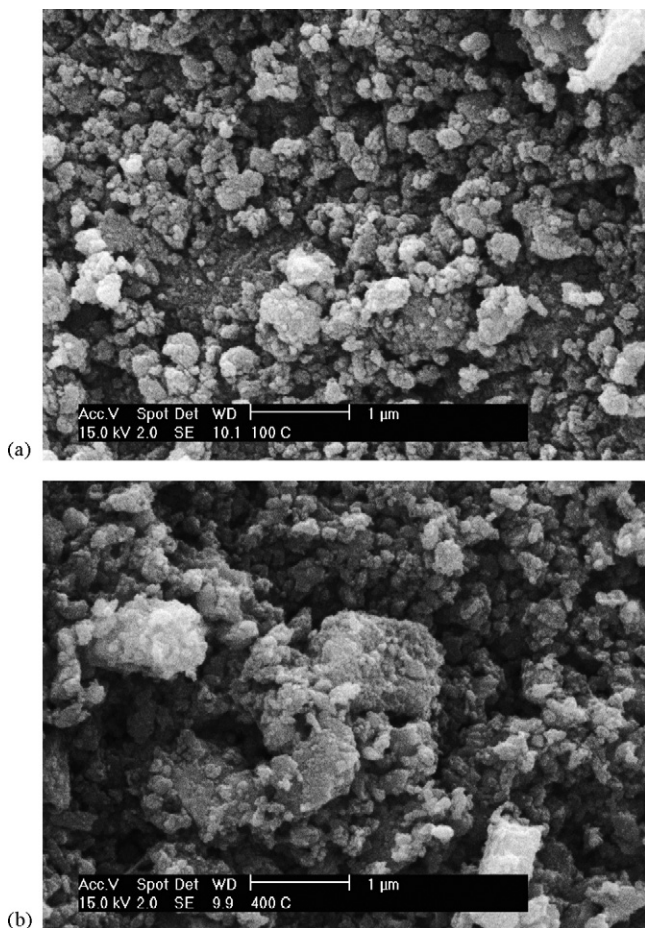Fig. 4. Pyrolusite fraction (P_r) within the heat treated EMD samples.

(a)

(b)

Fig. 6. SEM images of EMD heat treated at: (a) 100 °C and (b) 400 °C.

The first analysis of the data that can be conducted is determination of the surface area using the linearized BET isotherm [16]; i.e.

$$\frac{x}{V_a(1-x)} = \frac{1}{V_m C} + \frac{(C-1)x}{V_m C} \qquad (3)$$

where $x = P/P_0$, V_a the volume of gas adsorbed at x (cm³ g⁻¹), V_m the volume of gas that would occupy a monolayer (cm³ g⁻¹), and C a constant for the gas/solid pair. From a plot of $x/V_a(1-x)$ versus x, V_m can be determined from which the surface area (S; m² g⁻¹) can be calculated using the expression $S = 4.35 V_m$, in which case the factor of 4.35 takes into account the cross-sectional area of the adsorbing N_2 molecule (16.2 Å²) and various other conversion factors. The BET isotherm can only really be considered valid over the partial pressure range from 0.05 to 0.30 because at low partial pressures the isotherm under-predicts actual adsorption due to higher than expected gas adsorption energies on the solid as a result of surface inhomogeneity, while at relatively high partial pressures the BET isotherm over-predicts adsorption due to limitations associated with liquefication of the adsorbate [15]. BET surface areas of the heat-treated EMD samples, determined using Eq. (3), are shown in Fig. 8 as a function of the heat-treatment temperature. Firstly, the surface area of these samples are relatively high, much greater than the geometric surface area predicted from
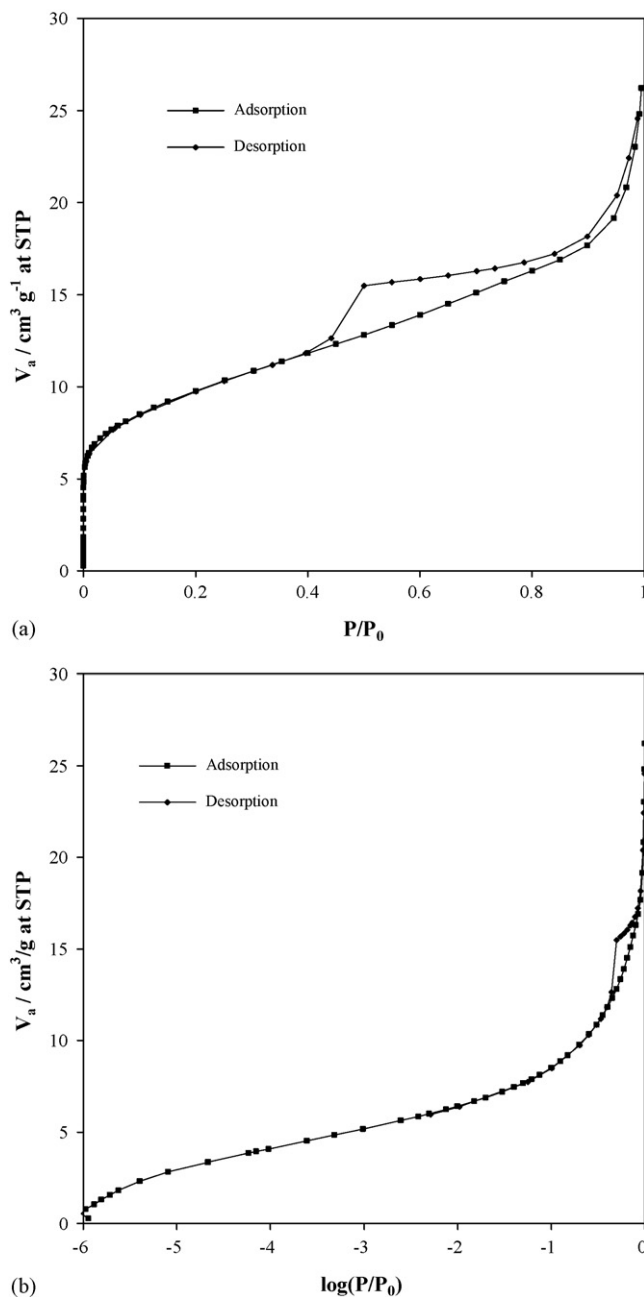

(a)

(b)

Fig. 7. Gas adsorption and desorption isotherms for the starting EMD used in this work. (a) Linear and (b) logarithmic P/P_0 data.

the particle size distribution. This of course indicates that the materials are quite porous. Secondly, note that the calculated surface area decreases progressively as the heat-treatment temperature is increased, particularly at the highest temperature, in which case the surface area decreases by ∼50%. Given the structural changes that are occurring upon heat-treatment, with the corresponding diffusion of Mn^{4+} ions through the oxygen anion framework, the decrease in surface area suggests that EMD pores are being sintered shut, essentially further crystallizing the material structure. This will of course be confirmed by examining the changes in pore size distribution with heat treatment.

There are of course alternative isotherms, other than BET theory, that can be used to describe gas adsorption on a solid
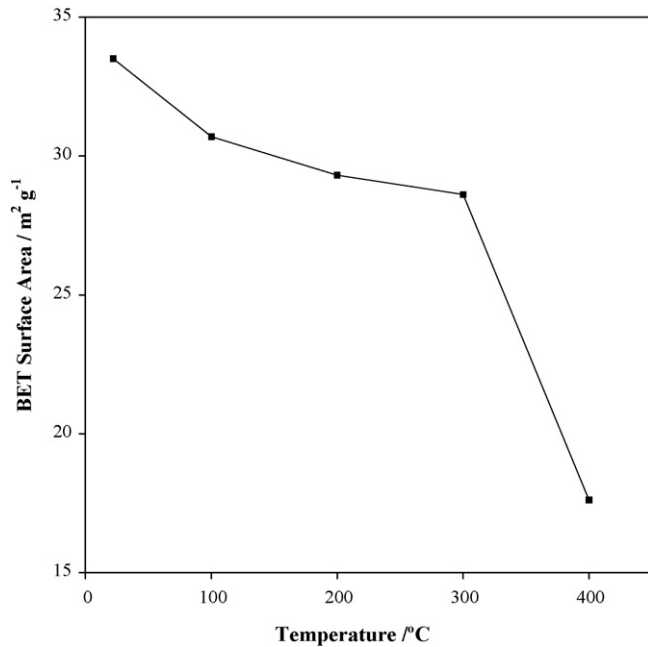
Fig. 8. BET surface areas of samples prepared in this work.

Fig. 9. Example of a t-plot using the FHH and HJ models (Eqs. (6) and (7), respectively).

substrate. One such approach is the Frenkel, Halsey and Hill (FHH) isotherm [17]:

$$\frac{V_a}{V_m} = \left[\frac{a}{\ln(P_0/P)}\right]^b \tag{4}$$

where a and b are empirical constants determined by fitting the isotherm to the experimental data. Another is the Harkins and Jura (HJ) isotherm [18]:

$$\frac{V_a}{V_m} = \left[\frac{a'}{b' - \log(P/P_0)}\right]^{0.5} \tag{5}$$

where a' and b' are again empirical constants. What is apparent about these two isotherms is that V_m cannot be determined directly, and hence the surface area cannot be estimated from these isotherms alone. However, if we were to employ the values of V_m obtained from the BET analysis, then estimates of the empirical constants a and b (or a' and b') can be made by fitting either Eq. (4) or (5) to the experimentally obtained adsorption data (Table 1). The partial pressure range over which the isotherms were fit was 0.05–0.85, and as can be seen in Table 1 from the r^2 values, the fit over this range was excellent in both cases. Outside of this partial pressure range significant devi-
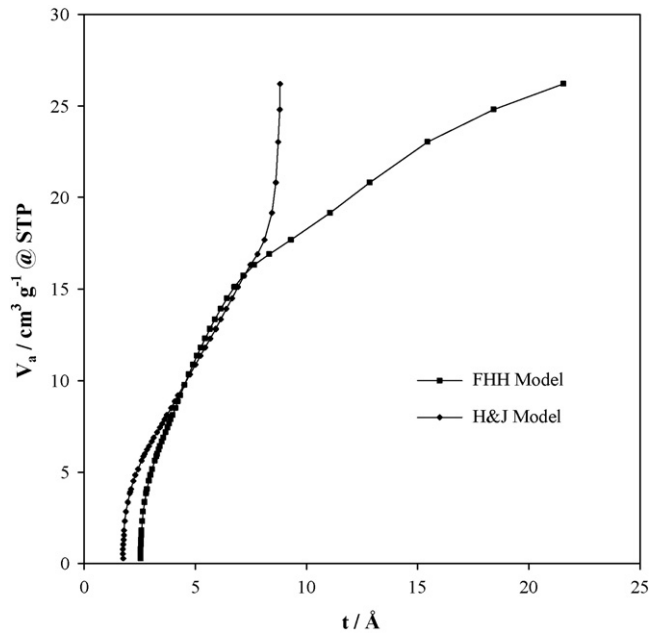
ation between the experimental and predicted isotherms was observed.

The significance of the FHH and HJ isotherms is that they allow us to determine the statistical thickness of the adsorbate (*t*), which in turn can be used to estimate the pore size distribution of the solid. Knowing V_a/V_m, which is the relative volume of gas adsorbed compared to the monolayer volume, the layer thickness can be determined using:

$$\text{FHH } t \text{ values}: \quad t = 3.54\left[\frac{a}{\ln(P_0/P)}\right]^b (\text{Å}) \tag{6}$$

$$\text{HJ } t \text{ values}: \quad t = 3.54\left[\frac{a'}{b' - \log(P/P_0)}\right]^{0.5} (\text{Å}) \tag{7}$$

where 3.54 Å corresponds to the thickness of a N_2 layer. An example of such a t-plot is shown in Fig. 9, which uses the absorption data for the starting EMD. Of course the data in Fig. 9 does not have much significance below a t value of 3.54 Å since this is the thickness of a N_2 monolayer. However, what it does indicate is that there is only partial coverage of the surface with N_2 molecules. Above 3.54 Å we have greater than a monolayer coverage, with the t value indicating the average N_2 thickness.

Table 1
Empirical parameters for the FHH and HJ isotherms

Sample	V_m (cm^3 g^{-1} at STP)	FHH			HJ		
		a	b	r^2	a'	b'	r^2
EMD	7.70	4.011	0.267	0.982	1.513	0.242	1.000
100 °C	7.06	3.819	0.295	0.971	1.448	0.185	1.000
200 °C	6.74	3.079	0.362	0.978	1.239	0.093	0.997
300 °C	6.58	2.717	0.428	0.991	1.133	0.037	0.998
400 °C	4.05	2.196	0.548	0.993	0.968	−0.018	0.998

3.3. Pore size distributions

Many different methods for assessing the porosity of solid materials from gas adsorption and desorption data have been proposed. Methods specific for meso- and macro-porous materials, as well as micro-porous materials have been reported and used extensively. In general, these methods of analysis are quite empirical in nature, and in some instances have flawed assumptions, but nevertheless they still find widespread use despite these shortcomings.

3.3.1. Using the Kelvin equation

For porous materials the Kelvin equation has been used extensively despite being relevant for only meso- and macro-porous materials [15,19]. The premise underlying this method is that the vapour pressure of the adsorbate in equilibrium with condensed adsorbate in the pores is less than P_0 as on a flat surface. On changing the external pressure, gas will adsorb or desorb from the available free surface, and when a suitable pressure is reached the centre of the pore will either fill from an adsorbed layer on the pore walls, or empty leaving behind an adsorbed layer. For cylindrical pores, the radius of pores is given by the sum of the statistical thickness t, as determined using thickness equations such as in Eqs. (6) and (7), and the Kelvin radius; i.e.

$$\ln\left(\frac{P}{P_0}\right) = -\frac{2\gamma V_L \cos\theta}{RTr_m} \tag{8}$$

where γ and V_L are the surface tension and molar volume of the condensed liquid adsorbate, θ the contact angle between the solid and condensed phase (for N_2 as the adsorbate, $\theta = 0°$ and so $\cos\theta = 1$), r_m is the radius of curvature of the meniscus, while R and T have their usual significance.

Using such an approach, the calculated pore size distribution for our heat treated series of EMDs is shown in Fig. 10. Using this method it is not straightforward to extract the behaviour of the micro-pores (<20 Å) as the initial EMD is heat treated. In some ways this was expected given that the use of the Kelvin equation is most relevant for meso-pores (20–500 Å) and macro-pores (>500 Å). Above 20 Å the resolution of the pore size distribution becomes sufficient such that we can extract meaningful information. What Fig. 10 suggests is that with heat treatment of EMD the pore volume (V_p) increases at larger pore sizes as the heat treatment temperature increases. As suggested previously, the reason for this is as the heat treatment temperature increases, the mobility of manganese ions in the structure increases to the point where the smaller pores within the structure are being sintered shut as a result of ion movement. However, with ion movement comes a structural rearrangement from γ-MnO$_2$ to the more dense β-phase. This increase in density may causes a stress build up in the heat treated materials, which in turn induces the formation of more larger cracks (larger pores) within the material.

One of the objectives of this work was to compare various methods of pore size analysis to confirm the trends we observe using any particular method. To do this correctly we must understand the various pitfalls associated with each method. The Kelvin method has been found to break down when P/P_0 reaches
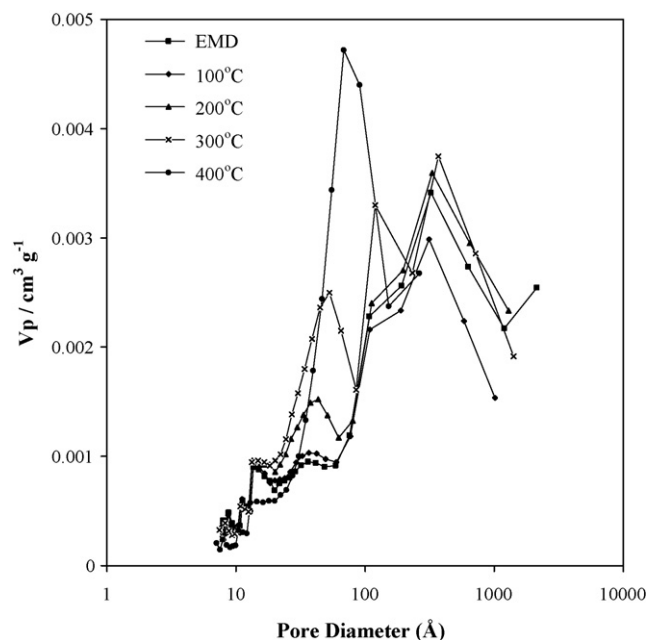

Fig. 10. Pore size distribution determined using the Kelvin equation combined with HJ thickness (t) data.

about 0.4 because the liquid nitrogen cannot support the high pressure differential of over 0.5 atm [20]. As a result, many materials appear to have a lot of pores at about 40 Å, when in fact it is a breakdown of the assumption of liquid behaviour that is being measured and actual pore sizes may be significantly smaller. For the data presented in Fig. 10, the peak in pore volume occurs around 40 Å bringing into question the validity of the calculated distribution. However, a redeeming feature of our data is the fact that an adsorption isotherm was used, which in effect avoids the hysteresis loop apparent in the desorption isotherm that gives rise to the overestimation of 40 Å pores.

While use of the Kelvin equation focuses primarily on larger pore sizes, as is clear from the results in Fig. 10, alternative methods have been developed to examine the smaller micro-pores. As we shall see these methods are quite empirical in nature, and as such the quality of results can be quite limited. This is particularly true for micro-porous materials where pore sizes are comparable to adsorbate dimensions.

3.3.2. MP method

The MP method of pore analysis [21] also makes use of the adsorbate thickness data described previously. From a plot of volume of gas adsorbed (V_a) versus the statistical thickness (t) the pore size distribution can be extracted by determining the equation of the tangent at each t value. The value of the tangent slope corresponds to the total micro-pore area in unfilled pores up to that t value. The pore volume (V_p) at this point can be determined from:

$$V_p = \left[\frac{(S_n - S_{n+1})(t_n + t_{n+1})}{2}\right] K \tag{9}$$

where S_i is the slope of the tangent at thickness t_i, and K is a constant converting gas volume at STP to liquid volume,
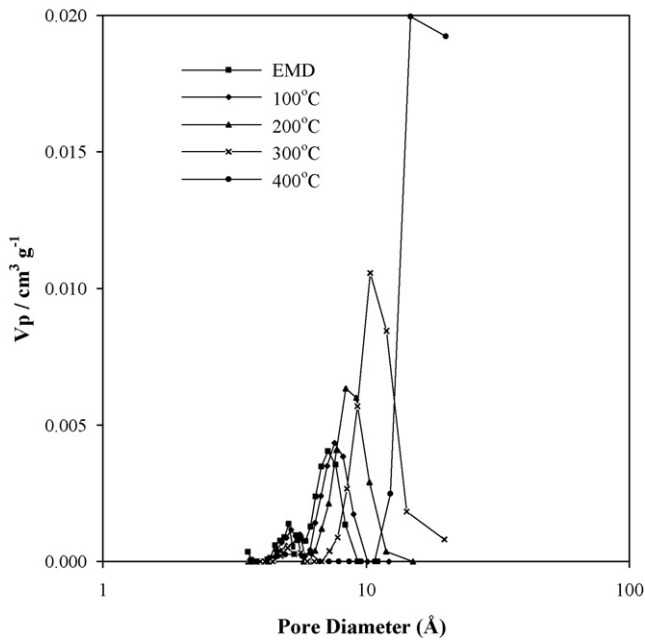
Fig. 11. Pore size distribution calculated using the MP method and FHH thickness data.

and Å to cm. The data in Fig. 11 show the results of using such an approach (combined with the FHH thickness data) to determine the pore size distribution. Similar trends can be observed with the use of HJ thickness data. In many ways the data in Fig. 11 confirms our model of structural change. Namely, as the heat treatment temperature increases the pore volume associated with very small pores decreases, as seen in the data at ∼5 Å. Furthermore, the pore volume associated with slightly larger pores (∼7 Å in the initial EMD, up to ∼15 Å for the sample with the highest heat treatment temperature) also increases with heat treatment temperature. Compared to using the Kelvin method, these trends in pore size distribution are similar but cover different pore size ranges, and so are not directly comparable. Nevertheless, the similarities do give us some confidence.

3.3.3. Dubinin–Radushkevich (DR) and Dubinin–Astakhov (DA) methods

While the concept of multi-layer gas adsorption on flat surfaces and the walls of large pores is valid, it is not necessarily appropriate when the pores themselves are comparable in size to adsorbate molecular dimensions. This led Dubinin and Radushkevich [19,22] to develop the following empirical expression for the filling of pores in microporous carbons; i.e.

$$V = V_0 \exp\left[-\left(\frac{A}{\beta E_0}\right)^2\right] \tag{10}$$

where V is the volume adsorbed at P/P_0 and temperature T, V_0 the limiting micro-pore volume, E_0 the characteristic adsorption energy of the reference material, β the affinity coefficient of the adsorbate for the solid surface, and A is the adsorption potential

given by

$$A = -\Delta G = RT \ln\left(\frac{P_0}{P}\right) \tag{11}$$

Combining Eqs. (10) and (11) and then rearranging gives:

$$\ln V = \ln V_0 - \left(\frac{RT}{\beta E_0}\right)^2 \ln^2\left(\frac{P_0}{P}\right) \tag{12}$$

from which a plot of $\ln V$ versus $\ln^2(P_0/P)$ should give a straight line, the Y-intercept of which is $\ln V_0$, which allows the limiting micro-pore volume for each sample to be determined after converting volume of gas adsorbed to liquid volume. Fig. 12(a)
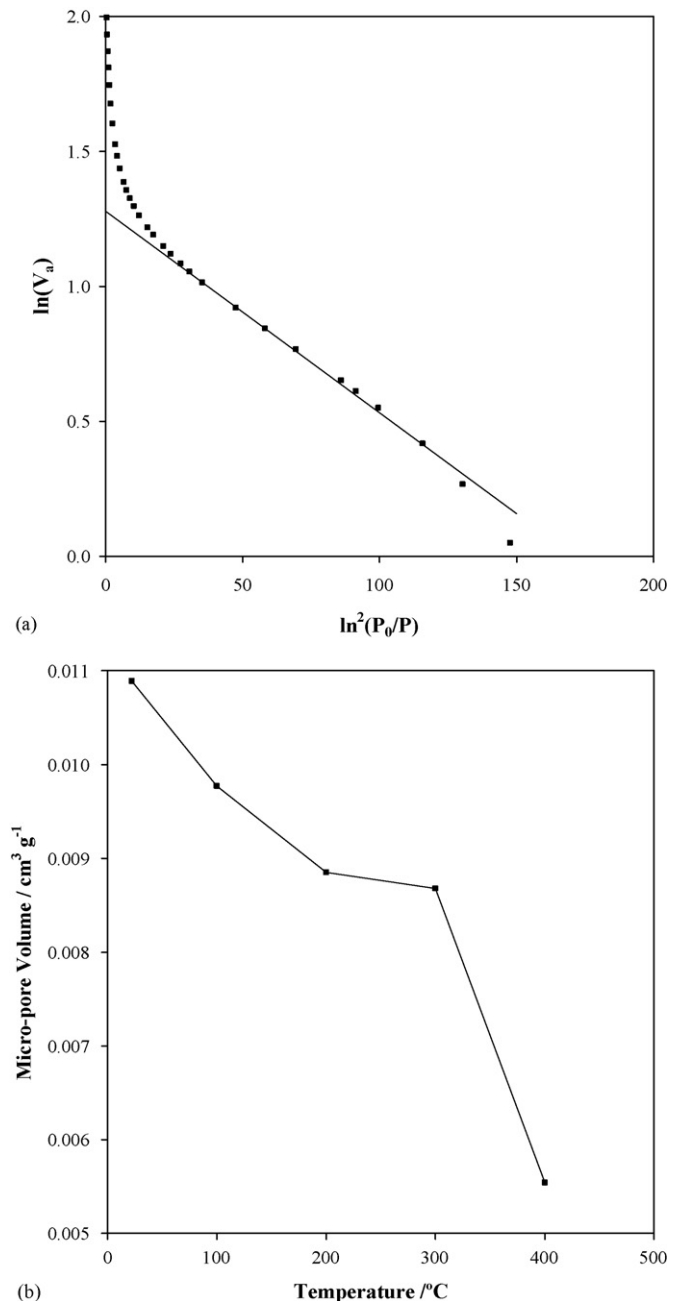

(a)

(b)

Fig. 12. (a) Dubinin–Radushkevich method of micro-pore volume analysis and (b) changes in EMD micro-pore volume with heat treatment.

shows a plot of Eq. (12) for the 400 °C heat treated sample, while Fig. 12(b) shows the changes in limiting micro-pore volume with heat treatment temperature. What is apparent firstly in Fig. 12(a) is the only partial linearity of the complete data set. Evidently at both low and high $\ln^2(P_0/P)$ values there is substantial deviation from the model. These regions of the data correspond to high and low partial pressure adsorption data, respectively, which for many other adsorption isotherm models, are regions were model breakdown also occurs. For the DR model this non-linearity has been noted before [19], with the significance of the results being subject to considerable debate. Nevertheless, using our best estimate of the linear region in the plot of Eq. (12) to generate the data in Fig. 12(b), we can see that the limiting micro-pore volume follows a trend that is remarkably similar to the changes in BET surface area for our samples. Assuming that the empirical nature of the DR method is legitimate for these samples, then we can firstly confirm that the bulk of EMD surface area is indeed associated with micro-porosity. Secondly, the data in Fig. 12(b) again supports our collapsing pore model for EMD heat treatment.

The Dubinin–Astakhov (DA) method [19,23] of micro-pore analysis is very similar to the DR method, except an additional degree of freedom is added to the volume filling expression; i.e.

$$V = V_0 \exp\left[-\left(\frac{A}{\beta E_0}\right)^n\right] \tag{13}$$

Here the value of n is selected to give the best fit of the model to the data, with again V_0 being the analysis result. As has been reported previously [19], the value of n was close to 2 for each sample, with the end result being that the micro-pore volume followed the same trends as those obtained for the DR method (Fig. 12(b)).

3.3.4. Density functional theory (DFT) based models

As we have seen above, conventional methods of determining a pore size distribution from gas adsorption and desorption data are quite empirical in nature. This is particularly true for microporous materials where pore sizes are comparable to adsorbate dimensions. A more recent advance [19] is to model the distribution of gas molecules in the system consisting of a gas and solid adsorbent using first principles; i.e., molecular dynamics or the Monte-Carlo methods. Another, less calculation intensive method involves using density functional theory (DFT) to describe this distribution. Despite being less demanding from a calculation perspective, the use of DFT provides an excellent representation of such an inhomogeneous system. Micromeritics DFT Plus v2.00 is an example of software that employs the DFT methodology. Essentially the software has a library of standard isotherms that have been calculated using the DFT methodology. These standard isotherms are specific for various gas-solid couples, as well as for certain pore shapes and sizes. The software then adjusts the relative contributions of these standard isotherms to fit to the experimental data, hence giving rise to an pore size distribution. The pore size distribution using such an approach, assuming slit shaped pores, is shown in Fig. 13.
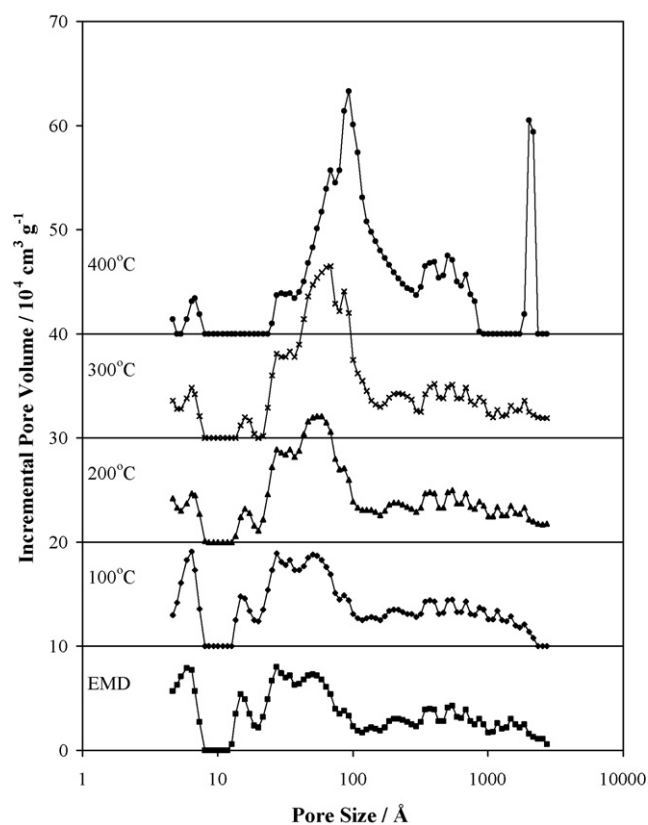

Fig. 13. Pore size distribution of the heat treated EMD series as determined using a DFT based method.

What is immediately obvious with this pore size distribution data is the enhanced resolution that is available, covering around three orders of magnitude of pore sizes. In terms of what the data represents, it is again consistent with our proposed model for structural and morphological change. At very small pore sizes (∼6 and ∼15 Å) heat treatment causes a considerable decrease in the adsorbed volume associated with these pore sizes. The pore volume associated with the slightly larger 30 Å pores is interesting in that it remains relatively constant with heat treatment, except at the highest temperature (400 °C) where it seems as though a number of these pores have been closed down. At larger pore sizes (>50 Å) there is a steady increase in pore volume due to stress-induced cracking as a result of material density differences, as has been discussed previously.

4. Summary and conclusions

A series of heat-treated EMD samples (100° to 400 °C) have been prepared and characterized using a collection of physical methods to evaluate the structural and morphological changes that have occurred as a result of heat treatment. The key conclusions that can be made from this work are:

(i) The structure of the starting EMD (γ-MnO$_2$) undergoes structural contraction along both the a and b axes, but expansion along the c axis. This has been explained in terms of the thermal diffusion of manganese ions (both Mn(IV)

and Mn(III)) resulting in a denser, less defective β-MnO_2 structure.

(ii) As a result of this manganese ion movement under heat treatment, micro-pores within the solid are sintered shut, the net result of which is a considerable decrease in the surface area.

(iii) The structural transition on heat treatment from γ- to β-MnO_2 also brings about an increase in material density. The structural contraction that occurs as a result has been found to induce cracking which causes an increase in the number of larger pores.

Acknowledgements

References

[1] R.G. Burns, V.M. Burns, Proc. MnO_2 Symp. 1 (1975) 306;
V.M. Burns, R.G. Burns, W.K. Zwicker, Proc. MnO_2 Symp. 1 (1975) 288.

[2] R. Giovanoli, in: I.M. Varentsov, G. Grasselly (Eds.), Geology and Geochemistry of Manganese, vol. 1, Akademiai Keadó, Budapest, 1980, p. 159.

[3] P.M. De Wolff, Acta Cryst. 12 (1959) 341.

[4] P. Ruetschi, J. Electrochem. Soc. 131 (1984) 2737;
P. Ruetschi, J. Electrochem. Soc. 135 (1988) 2657;
P. Ruetschi, R. Giovanoli, J. Electrochem. Soc. 135 (1988) 2663.

[5] Y. Chabre, J. Pannetier, Prog. Solid State Chem. 23 (1995) 1.

[6] C. Kim, Z. Akase, L. Zhang, A.H. Heuer, A.E. Newman, P.J. Hughes, J. Solid State Chem. 179 (2006) 753.

[7] C.B. Ward, A.I. Walker, A.R. Taylor, Prog. Batt. Batt. Mater. 11 (1992) 40.

[8] S. Turner, P.R. Buseck, Science 203 (1979) 456.

[9] A.H. Heuer, A.Q. He, P.J. Hughes, F.H. Feddrix, ITE Lett. Batt. New Technol. Med. 1 (2000) 926.

[10] A. Kozawa, R.A. Powers, J. Electrochem. Soc. Jpn. 37 (1969) 31;
A. Kozawa, J.F. Yeager, J. Electrochem. Soc. 115 (1968) 1003;
A. Kozawa, R.A. Powers, J. Electrochem. Soc. 115 (1968) 122;
A. Kozawa, R.A. Powers, Electrochem. Technol. 5 (1967) 535;
A. Kozawa, R.A. Powers, J. Electrochem. Soc. 113 (1966) 870.

[11] S.W. Donne, G.A. Lawrance, D.A.J. Swinkels, J. Electrochem. Soc. 144 (1997) 2949.

[12] Z. Hong, C. Zhenhai, X. Xi, J. Electrochem. Soc. 136 (1989) 2771.

[13] F. Petit, J. Durr, M. Lenglet, B. Hannoyer, Mater. Res. Bull. 28 (1993) 959;
F. Tedjar, J. Guitton, Thermochim. Acta 181 (1991) 13.

[14] A.R. West, Solid State Chemistry and Its Applications, John Wiley and Sons, 1984.

[15] D.A.J. Swinkels, N. Bristow, R.P. Williams, Prog. Batt. Batt. Mater. 13 (1994) 12.

[16] S. Brunauer, P.H. Emmett, E. Teller, J. Am. Chem. Soc. 60 (1938) 309.

[17] G.D. Halsey, J. Chem. Phys. 16 (1948) 931;
T.L. Hill, Adv. Catal. 4 (1952) 211.

[18] G. Jura, W.D. Harkins, J. Chem. Phys. 11 (1943) 430;
W.D. Harkins, G. Jura, J. Chem. Phys. 11 (1943) 431;
W.D. Harkins, G. Jura, J. Am. Chem. Soc. 66 (1944) 1362;
W.D. Harkins, G. Jura, J. Am. Chem. Soc. 66 (1944) 1366.

[19] P.A. Webb, C. Orr, Analytical Methods in Fine Particle Technology, Micromeritics Corporation, 1997.

[20] S.J. Gregg, K.S.W. Sing, Adsorption Surface Area and Porosity, 2nd ed., Academic Press, London, 1982.

[21] R.Sh. Mikhail, S. Brunauer, E.E. Bodor, J. Coll. Interface Sci. 26 (1968) 45.

[22] M.M. Dubinin, L.V. Radushkevick, Doklady Akademii Nauk SSSR 55 (1947) 327.

[23] M.M. Dubinin, V.A. Astakhov, Izvestiya Akademii Nauk SSSR, Seriya Khimicheskaya 1 (1971) 5.